Deforming the Upper Mantle-Olivine Mechanical Properties and Anisotropy

Sylvie Demouchy, Qin Wang, Andréa Tommasi

Deforming the Upper Mantle: Olivine Mechanical Properties and Anisotropy

by Sylvie Demouchy[1], Qin Wang[2], and Andrea Tommasi[3]

Demouchy, S., Wang Q. and Tommasi, A. (2023). Driving Upper Mantle Flow - Olivine Mechanical Properties and Anisotropy. *Elements*. 19, 151-157. doi: 10.2138/gselements.19.3.151

ABSTRACT

The interior of the Earth remains our last *terra incognita*, inaccessible to direct observations. Our understanding of the deformation of the mantle, which shapes our planet through convection and plate tectonics, is based on analysis of: (1) rare mantle rocks carried to the Earth's surface by volcanic or tectonic processes, (2) the consequences of this deformation on the planet's surface, and (3) geophysical data. These observables combined with laboratory experiments and numerical modeling imply that olivine deforms via the motion of defects within its crystalline structure and along grain boundaries. Ductile deformation by these crystal-scale processes results in anisotropic propagation of seismic waves, which allows us to probe upper-mantle deformation at scales of tens to hundreds of kilometers.

KEYWORDS: rheology; defect motion; crystal preferred orientation; seismic anisotropy; water-weakening

---

[1] Laboratoire Magmas et Volcans
Université Clermont Auvergne
Campus Universitaire des Cézeaux
6 Avenue Blaise Pascal
63178 Aubière Cedex, France
E-mail: sylvie.demouchy@uca.fr

[2] State Key Laboratory for Mineral Deposits Research
School of Earth Sciences and Engineering
Nanjing University
Nanjing 210023, China
E-mail: qwang@nju.edu.cn

[3] Géosciences Montpellier
CNRS & Université de Montpellier
Montpellier, France
E-mail: andrea.tommasi@umontpellier.fr

HOW DOES OLIVINE DEFORM?

Olivine is the most abundant mineral (>60 vol.%) in the Earth's upper mantle. The slow and continuous deformation (creep) of mantle rocks is therefore controlled by the ability of olivine to deform. A reference parameter to understand how olivine deforms in the deep Earth is the homologous temperature, which is defined as the ratio of temperature T to the melting temperature (solidus) Tm of a crystalline material in Kelvin. The asthenospheric part of the upper mantle is the weakest, as the geotherm is the closest to the solidus. Similar to metals or ice, olivine can experience ductile deformation (without loss of material continuity) when the homologous temperature (T/Tm) is higher than 0.4 at mantle pressures (>1GPa) (Wang 2016). The melting temperature of dry olivine with a typical mantle composition (Fo90) is Tm = 2053 K (1780 ÅãC) at 0.1 MPa. Thus, T/Tm = 0.4 corresponds to a temperature of 821 K. This low temperature limits the ductile deformation of olivine and is consistent with the absence of intraplate oceanic earthquakes at depths below the ~600 °C

Point defects in the crystal lattice can be classified as vacancies (unoccupied lattice sites), interstitials (extra atoms between normal lattice sites), and substitutions (foreign atoms, see Jollands et al. 2023 this issue). Their interactions and equilibria are controlled by mass balance, lattice site balance, and electroneutrality (Nakamura and Schmalzried 1983; Jollands et al. 2023 this issue). Vacancies play a major role in deformation. Under differential stress, olivine may deform by (1) ionic diffusion of vacancies through the crystal lattice (Nabarro–Herring creep) and (2) ionic diffusion of vacancies along grain boundaries (Coble creep, Fig. 1A). In olivine, as in all silicates, Si^{4+} is the ionic species with the slowest diffusion rate. Thus, its self-diffusivity limits the diffusion creep rate, which has a positive dependence on temperature (and hydrogen concentration) but a negative dependence on pressure (e.g., Hirth and Kohlstedt 2003; Fei et al. 2013). During diffusion creep (Fig. 1A), grains tend to shorten parallel to the maximum compressive stress and lengthen parallel to the minimum compressive stress, forming a shape-preferred orientation. In nature, grain elongation is nevertheless limited by concomitant grain boundary migration aiming to decrease the grain boundary energy. Diffusive processes depend on the inverse of the grain size to a powe1 $<m \leq 3$; an increase in grain size therefore reduces strain rates in the diffusion creep regime (e.g., Kohlstedt 2006).

Olivine also deforms by the motion of translational linear defects through the crystal lattice. These defects are call dislocations. A dislocation is defined by two vectors (FIG. 1B): the line vector ***u,*** also called the dislocation line, and the Burgers vector ***b,*** which gives the slip direction and has a length of one lattice parameter (only [100] and [001] are commonly observed in olivine). Dislocations may be observed as straight lines displaying a clear edge (i.e., ***b*** perpendicular to ***l***)

or screw (i.e., $\boldsymbol{b}$ parallel to $\boldsymbol{l}$) character (FIG. 1B) or as curved segments or loops composed of edge, screw, and mixed segments). The motion of edge and screw dislocations results in shearing of the crystal perpendicular or parallel to the dislocation line, respectively. The combinations of slip directions [*uvw*] and slip planes (*hkl*) in which dislocations may glide through the crystal lattice define the possible slip systems in a crystal. Olivine only possesses three slip systems: [100](010), [100](001), and [001]{hk0}. In a crystalline aggregate such as a rock, deformation by motion of dislocations with a limited number of slip systems induces a rotation of the grain crystallographic lattices. It therefore produces a crystal preferred orientation (CPO), which progressively aligns the dominant slip system with the mantle flow direction and plane.

At low temperature ($<0.6T_m$) and high stress, ductile deformation of olivine occurs essentially by dislocation glide. However, interactions between dislocations hinder their motion and produce strain hardening. At higher temperature ($>0.6T_m$), edge dislocations can climb (i.e., move to another glide plane to avoid an obstacle) with the help of diffusion of specific vacancies called jogs. Climbing dislocations have more opportunity to annihilate with dislocations of opposite sign or to reorganize into lower energy configurations (subgrains). These mechanisms, which reduce the dislocation density in a crystal, are called "recovery". They prevent strain hardening and allow steady-state conditions to be reached. Strain hardening by accumulation of dislocations may also be avoided via recrystallization, which involves the formation and migration of grain boundaries. If this occurs syn-deformation, recrystallization is then called dynamic. Deformation by dislocation creep involves a combination of dislocation glide, climb, recovery processes, and dynamic recrystallization. This combination allows for steady-state conditions or even weakening. Dynamic recrystallization accelerates the evolution of the CPO at low strain and stabilizes it at high strain (e.g., Bystricky et al. 2000; Tommasi and Vauchez 2015). It also produces noticeable grain size reduction at low temperature and/or high stress, when strain rates are faster than grain boundary migration rates.

Grain boundaries also play an important role in the deformation of mantle rocks. Grain boundaries are interfaces with misorientations > 15° between adjacent crystals (FIG. 1C, *NB:* 15° is an arbitrary value, commonly used for mantle rocks). They are characterized by complex structures with significantly higher defect densities than grain interiors. The high densities of defects make grain boundaries easier paths for ionic diffusion. They are also sources or sinks of dislocations. Grains may also slide parallel to their boundaries (grain boundary sliding, FIG. 1C) or be sheared near the boundary (Cordier et al. 2014). These grain-boundary processes may be coupled to diffusion or dislocation motion. Diffusion-accommodated grain boundary sliding was, for instance, proposed to allow for superplasticity in the mantle with CPO formation (Miyazaki et al. 2013). Although it is the first process that comes to mind, grain boundary sliding is not the only

grain boundary mechanism assisting ductile deformation. Grain boundary migration plays an essential role in dynamic recrystallization (FIG. 1C) and, hence, in dislocation creep. In addition, processes such as coupled migration and shear due to motion of specific grain boundary defects (disclinations, see Cordier et al. 2014; and disconnections) or stress-induced grain boundary amorphization have been put forward, but require further investigation. Finally, under fluid- or melt-present conditions, mantle rocks may also deform via dissolution-precipitation creep, which requires the transport of components dissolved in a fluid percolating along grain boundaries (e.g., Hidas et al. 2016).

HOW DO WE MODEL OLIVINE DEFORMATION?

The different deformation mechanisms presented above are likely to operate simultaneously, which can be expressed by the following constitutive equation:

$$\dot{\varepsilon}_{bulk} = \dot{\varepsilon}_{diffusion} + \dot{\varepsilon}_{dislocation} + \dot{\varepsilon}_{grain\ boundary} \qquad (1)$$

where $\dot{\varepsilon}_{bulk}$ is the macroscopic strain rate. One mechanism often dominates the rheology of mantle rocks at a given range of temperature, pressure, differential stress, strain rate, and chemical environment (hydration and redox states). Traditionally, the relationship between the strain rate ($\dot{\varepsilon}$) and stress (σ) for steady-state creep involving dislocation creep, diffusion creep, and grain boundary processes is approximated by a generic semi-empirical formulation (power flow law, e.g., Hirth and Kohlstedt 2003):

$$\dot{\varepsilon}_{high\ temperature} = \mathrm{A}\, d^{-m}\, f_{\mathrm{H_2O}}^{r}\, \sigma^{n} \exp\left(\frac{-E+PV}{RT}\right) \qquad (2)$$

where d is the grain size and m its exponent, f_{H2O} is the water fugacity and r its exponent, σ is the stress and n its exponent, E is the activation energy per mole, P is pressure, V is the activation volume, and R is the gas constant. A is the pre-exponential constant that depends on the material and hides many parameters not explicitly controlled during the experiments (e.g., grain boundary thickness, vacancy and jog concentration, Si self-diffusivity, dislocation density and velocity). Note that m and n are essentially fitting parameters to experimental data, yet their variation ranges permit discrimination between dominant deformation mechanisms in the experiments.

Most deformation experiments on olivine have been carried out at high temperature using fine-grained (2–100 μm) sintered olivine aggregates. These experiments typically yield the following parametrizations, which allow discrimination between different dominant deformation mechanisms (Hirth and Kohlstedt 2003; Kohlstedt 2006). Diffusion creep is sensitive to grain size (m = 3) and has a linear viscous rheology (n = 1). Dislocation creep is independent of grain size (m = 0) and has a non-linear dependence on stress (n = 3.5 or 3 for dry and hydrated olivine,

respectively). Dislocation-accommodated grain boundary sliding is characterized by both a non-linear stress dependence ($n \approx 3$) and a lower influence of grain size on the strain rate ($m = 0.7$ for dry olivine; Hansen et al. 2011, and $m = 1.1$ for olivine containing 20–130 ppm H_2O wt.; Ohuchi et al. 2015).

The generic semi-empirical flow law given by Eq. (2) breaks down at the high stresses associated with deformation at $T < 0.7T_m$. Under such conditions, recovery processes are less effective, and stress plays an increasing role on the dislocation interactions. Experimental data are then better approximated by an exponential flow law (e.g., Demouchy et al. 2013):

$$\dot{\varepsilon}_{low\ temperature} = B \exp\left(\frac{-E}{RT}\left(1 - \left(\frac{\sigma}{\sigma_{\mathrm{Peierls}}}\right)^p\right)^q\right) \qquad (3)$$

where B is a material constant, again hiding many parameters, $\sigma_{\mathrm{Peierls}}$ is a stress barrier for dislocation motion (see online supplemental material), and p and q are fitting parameters.

These flow laws of olivine provide a base for modeling upper mantle dynamics, but they are obtained at laboratory strain rates of 10^{-4}–10^{-6} s^{-1} and need to be extrapolated to mantle strain rates of 10^{-14}–10^{-16} s^{-1}. As a first step to constrain this important extrapolation, Gouriet et al. (2019) modeled dislocation dynamics in an olivine crystal over a large range of strain rates (from laboratory rates to those prevailing on Earth) and temperatures between 800 and 1700 K. In these models, deformation is essentially produced by dislocation glide, but at a rate controlled by dislocation climb. Strain rates are thus controlled by both dislocation velocities and Si self-diffusivity, which are constrained by laboratory data. This study showed that the transition between the power and exponential laws is continuous at the microscopic scale, reconciled the low- and high-temperature ductile deformation of olivine single crystals, and proposed a unified flow law for dislocation creep (see online supplemental material for comparison between this flow law and previous formulations):

$$\dot{\varepsilon}_{unified\ dislocation\ creep} = B\left(\frac{\sigma}{\mu}\right)^n \exp\left(\frac{-E}{RT}\left(1 - \left(\frac{\sigma}{\sigma_{Peierls}}\right)^p\right)^q\right) \qquad (4)$$

where μ is the shear modulus and the other parameters are similar to those in Eqs. (2) and (3). Best fit parameters for an olivine crystal well-oriented to deform with major activation of the [001](100) system are $B = 1.7 \times 10^{-16}$ s^{-1}, $n = 2.95$, $\sigma_{\mathrm{Peierls}} = 2$ GPa, $p = 1.52$, and $q = 2$. Equation (4) yields a nonlinear rheology with a stronger dependence of the strain rate on stress at low temperature. This cannot be inverted analytically, but alternative mathematical formalisms (hyperbolic tangent parameterizations) have been proposed, allowing it to be implemented in geodynamical models (e.g., Garel et al. 2020).

WATER-WEAKENING PHENOMENON IN OLIVINE

The water-weakening phenomenon was first observed in quartz, showing a drastic drop in stress by one order of magnitude at constant strain rate, during compression experiments under hydrous conditions (Griggs 1967). Nine years later, the first interpretation was proposed based on observations in glasses: the hydroxylation of Si-O bonds accelerates the average velocity of mobile dislocations. Deformation experiments later demonstrated that hydrogen-doped olivine crystals and aggregates also show a drop in stress, but by a factor of two at constant strain rate. The current theoretical framework is provided in Kohlstedt (2006). The fundamental equation behind this effect states that the self-diffusivity of an ionic species (D_i) is proportional to the diffusivity of its vacancies (D_v) times their concentration [V] (see Nakamura and Schmalzried 1983).

$$D_i \propto D_v \times [V] \tag{5}$$

Due to mass balance and electroneutrality constraints, the addition of hydrogen, even at trace-element concentration levels, increases the concentration of Si vacancies, enhances Si self-diffusivity, and induces weakening during diffusion creep. Water-weakening also occurs in dislocation creep, where strain rate depends on both dislocation glide and climb velocities. The latter are controlled by jog mobility, which depends on the Si vacancy concentration and Si self-diffusivity (Kohlstedt 2006). A similar reasoning can be postulated for grain boundaries, with incorporation of hydrogen facilitating recrystallization, sliding, and migration. However, experimental data quantifying these effects in a robust manner are still missing.

The quantification of the water-weakening effect at deformation rates (10^{-14}–10^{-16} s^{-1}) and hydrogen concentrations (10–200 wt. ppm H_2O) relevant for the Earth's mantle remains an open question. A compilation of hydrogen concentrations in olivine (FIG. 2) implies that hydrogen concentrations are usually not high enough to produce significant water-weakening (cf. online supplemental material).

Furthermore, upon extrapolating the most recent dislocation creep flow laws for hydrogen-doped olivine single crystals combined with the low-temperature dislocation creep flow law (Tielke et al. 2017) to upper mantle strain rates, we can conclude that a significant water-weakening (effective viscosity drop of > 10; FIG. 3) is predicted at high strain rates (10^{-12} s^{-1}), but for a limited range of low temperatures (950–1100 °C, cf. online supplemental material). This extrapolation suggests that water-weakening might be only relevant for localized deformation in the mantle lithosphere, at plate boundaries for example. However, the impact of hydrogen stored at grain boundaries on the rheological properties of olivine-rich rocks still needs to be quantified.

PROBING MANTLE FLOW USING SEISMIC ANISOTROPY

Exposures of upper-mantle rocks (peridotites) at the Earth's surface by tectonic or magmatic processes are rare but valuable. The study of these rocks constrains: (1) the deformation mechanisms involved in the lithospheric and shallow asthenospheric mantle, (2) possible interactions between deformation and fluids or magma transport, and (3) deformation patterns up to the kilometer scale. However, even the largest peridotite massifs, like the mantle section of the Oman ophiolite, with outcrops over 500 km^2, are only fossil testimonies of past deformation, extracted from their original context.

In situ observation of deformation and first-order mapping of the flow patterns in the upper mantle are possible using seismological data due to: (1) the strong elastic anisotropy of olivine (Abramson et al. 1997) and (2) mantle deformation producing coherent crystal preferred orientation (CPO, see above) of olivine at the scales sampled by seismic waves (tens of kilometers). This approach was pioneered by Hess (1964), who interpreted variations in sub-Moho P-wave velocities in different directions along refraction profiles as recording past ridge dynamics related to flow patterns frozen in the shallow mantle of the Pacific plate. Since then, measurement of seismic anisotropy, that is, velocity variations of seismic waves as a function of their propagation or polarization direction (FIG. 4), has been recognized as the most effective tool to probe past and present-day upper-mantle flow patterns.

Yet at face value, deduction of mantle flow patterns from seismic anisotropy data is not straightforward because it depends on: (1) the relationship between seismic anisotropy and olivine CPO or other structures that may produce large-scale seismic anisotropy, such as oriented melt pockets, and (2) the relationship between the CPO and deformation. As multiple processes or deformation geometries may produce similar seismic anisotropy signatures, the latter cannot be inverted to obtain unique flow patterns. Moreover, in most cases, seismological data only sample part of the elastic stiffness tensor and integrate data along the seismic wave path.

Fortunately, analysis of > 700 naturally deformed peridotites extracted from the lithospheric and shallow asthenospheric mantle in varied geodynamical settings revealed that 95% of the samples display olivine CPO characterized by dominant orientation of the [100] axes within the flow plane, with a maximum parallel to the flow direction (FIG. 5). Similar olivine CPO develops during simple shear and compression experiments at high temperature, moderate pressure, and low water content (e.g., Bystricky et al. 2000). This dominant olivine CPO in nature establishes a simple relationship between flow geometry and seismic anisotropy orientation: fast polarization directions of teleseismic S waves and fast propagation of P and Rayleigh waves indicate the flow direction (FIG. 4). We recall that when an S wave enters an anisotropic medium, it is split in two quasi-S waves polarized in perpendicular planes, which have different velocities ($Vs1 > Vs2$). This

phenomenon is called S-wave splitting. The delay time between the arrival of the fast S1 and slow S2 waves is a measure of the intensity of the anisotropy. Because it relates to the CPO concentration, it is tempting to interpret the intensity of seismic anisotropy as recording deformation intensity. However, this is not possible because CPO evolution saturates at low strain and depends on the initial state. One should not forget that probably none of the present-day mantle is pristine or undeformed. Moreover, the anisotropy intensity also depends on how the seismic waves sample the anisotropic rock layer (pathlength and direction).

The simple relationship between flow geometry and seismic anisotropy presented above may break down in the deep upper mantle, forearc sections of the mantle wedge, and shear zones in the shallow lithospheric mantle because in these settings, high pressure, hydration status, or high stress may induce changes in olivine's dominant slip systems, favoring glide along [001] relative to [100] (e.g., Couvy et al. 2004; Jung and Karato 2001). Such a change in the dominant slip system results in a concentration of [001] parallel to the flow direction and fast propagation of P waves and polarization of S waves normal to the flow direction. This may explain the change in orientation and decrease of seismic anisotropy in the upper mantle below 250 km (Mainprice et al. 2005). Moreover, it may also reconcile trench-parallel, fast S-wave polarization directions with trench-normal corner flow in the mantle wedge. Such olivine CPO is rare in natural mantle specimens as illustrated in FIG. 5, being only observed in high-pressure peridotite massifs associated with eclogites, which record deformation under high-pressure conditions (e.g., Frese et al. 2003). Layering and CPO of hydrous minerals, like serpentine or chlorite, may alternatively explain trench-parallel anisotropy in forearc regions (e.g., Boudier et al. 2010). High-stress deformation could produce fast shear-wave polarization normal to the flow direction in the shallow sections of shear zones crosscutting the lithospheric mantle. However, samples from this type of shear zone show evidence for extensive recrystallization, leading to grain size reduction and a significant contribution of fluid-assisted grain boundary processes. These samples usually display weak olivine CPO and seismic anisotropy (e.g., Hidas et al. 2016).

Simple shear experiments with 3%–30% anhydrous melt fractions also produced alignment of olivine [001] axes subparallel to the shear direction and [010] axes subnormal to the shear plane, which was attributed to strain partitioning between melt-rich layers and melt-depleted lenses (Holtzman et al. 2003). However, natural peridotites deformed in the presence of melts show dispersion of [100] axes in the flow plane, without preferred alignment of [001] parallel to the flow direction (anhydrous basaltic melts, Higgie and Tommasi 2012) or extremely weak olivine CPO (hydrous melts). A weak preferred orientation of olivine [001] axes parallel to the lineation has nevertheless been described in cumulative dunites deformed by compaction of a crystal–magma mush (Yao et al. 2019). Yet, seismic anisotropy associated with these CPOs are only

observed seismically if the melts are extracted or crystallized. When melts are present, their effect overcomes that of the olivine CPO and S-wave velocities strongly decrease as a function of the melt concentration. Furthermore, deformation-induced preferred orientation of melts in layers at low angle or parallel to the shear plane promotes strong seismic anisotropy with fast S-wave polarization and P-wave propagation directions parallel to the shear plane.

Diffusion creep probably predominates in slowly deforming sections of the convective upper mantle. How does this affect the seismic anisotropy signal? Traditionally, diffusion creep was considered to not produce the CPO. Moreover, recent deformation experiments suggest that diffusion creep can produce weak olivine CPO with similar relationships to the flow pattern as those developed during dislocation creep under high-temperature and low-stress conditions (Miyazaki et al. 2013). Thus, the presence or absence of seismic anisotropy cannot be used to map transitions between dislocation and diffusion creep in the upper mantle.

SYNTHESIS: OLIVINE AND UPPER MANTLE DEFORMATION

The current evidence from deformation experiments does not always explain the observations on olivine-rich rocks. Nevertheless, some points can be asserted. (1) Analyses of natural peridotites imply that in the lithospheric mantle and shallow asthenosphere, the dominant deformation mechanism is dislocation creep of olivine. (2) By combining experimental results and numerical models, we now have a unified flow law to describe dislocation creep over the entire lithospheric and asthenospheric mantle. (3) Incorporation of hydrogen in the olivine structure could lower the strength of mantle rocks and change the relationship between seismic anisotropy and flow direction. However, evidence for a change in the dominant slip system due to hydrogen incorporation remains rare among naturally deformed peridotites (FIG. 5). In addition, extrapolation of the most recent experimental data to natural strain rates predicts no major water-weakening in the lithospheric mantle, except in highly localized shear zones if olivine contains hydrogen (FIG. 3). (4) The ever-growing database of geophysical measurements of seismic anisotropy is a unique tool to probe in situ upper mantle flow patterns (FIG. 4). The predominance of dislocation creep by [100] glide results in a simple relationship between olivine CPO and the seismic anisotropy of peridotites, which usually allows mantle flow directions to be determined from seismic anisotropy data. This simple relationship may nevertheless be questioned in domains that deform at high stresses, in the deep upper mantle (high pressure), and when olivine may hold a high hydrogen concentration. However, because multiple processes can produce similar seismic anisotropy signatures, seismic anisotropy data cannot be unequivocally inverted to infer the active or ancient deformation processes in the mantle or physio-chemical conditions of deformation. (5) The fundamental mechanisms of olivine deformation are not yet

fully understood, especially grain boundary–based mechanisms and the impact of microstructure evolution on the mantle rheology with time.

FUTURE OUTLOOKS

The multi-method approach presented here has not reached its limits. Further laboratory experiments should be conducted to explore how the rheology of upper-mantle rocks may evolve with time or strain. Novel approaches to unravel the olivine deformation mechanisms and anisotropy of physical properties include the use of in situ micro-mechanical tests to provide information on defect interactions in olivine, experiments on analog materials, and numerical modeling techniques, such as artificial intelligence, to quantitatively predict ductile deformation and its anisotropy. Numerical modeling at a large scale still has a role to play by exploring the types of feedback that are impossible to track in laboratory experiments, including those associated with changes in the dominant deformation mechanisms, water-weakening, and presence of fluids/melts in the mantle. Olivine has yet to reveal all its secrets.

ACKNOWLEDGEMENTS

The authors thank Anne Delplanque and Catherine Thoraval for help with figures. The authors acknowledge funding from CNRS-INSU though their program TELLUS-Syster (DOMINO 2021–2022) in France, the National Science Fund for distinguished young scholars in China (No. 41825006), and the European Research Council (ERC) under the European Union's Horizon 2020 research and innovation program under grant agreement No 882450 – RhEoVOLUTION.

ONLINE SUPPLEMENTS

1. Methodology for unified dislocation creep flow law for Eq. (4)

2. Data source and methodology for FIG. 2

3. Methodology for FIG. 3

4. Data source for FIG. 4

REFERENCES

Abramson EH, Brown M, Slutsky LJ, Zaug J (1997) The elastic constants of San Carlos olivine to 17 GPa. Journal of Geophysical Research 102: 12253-12263, doi: 10.1029/97JB00682

Barruol G, Wuestefeld A, Bokelmann G (2009) SKS-splitting-database. Université de Montpellier, Laboratoire Géosciences, doi: 10.18715/sks_splitting_database

Boudier, F, Baronnet A, Mainprice D (2010) Serpentine mineral replacement of natural olivine and their seismic implications: oceanic lizardite versus subduction-related antigorite. Journal of Petrology 51: 495-512, doi: 10.1093/petrology/egp049

Bystricky M, Kuntze K, Burlini L, Burg J-P (2000) High shear strain of olivine aggregates: rheological and seismic consequences. Science 290: 1564-1567, doi: 10.1126/science.290.5496.1564

Cordier P and 5 coauthors (2014) Disclinations provide the missing mechanism for deforming olivine-rich rocks in the mantle. Nature 507, 51-56, doi: 10.1038/nature13043

Couvy H and 6 coauthors (2004) Shear deformation experiments of forsterite at 11 GPa – 1400C in the multianvil apparatus. European Journal of Mineralogy 16: 877-889, doi: 10.1127/0935-1221/2004/0016-0877

Demouchy S, Bolfan-Casanova N (2016) Distribution and transport of hydrogen in the lithospheric mantle: a review. Lithos 240-243: 402-425, doi: 10.1016/j.lithos.2015.11.012

Demouchy S, Tommasi A, Boffa Ballaran T, Cordier P (2013) Low strength of Earth's uppermost mantle inferred from tri-axial deformation experiments on dry olivine crystals. Physics of the Earth and Planetary Interiors 220: 37-49, doi: 10.1016/j.pepi.2013.04.008

Fei H, Wiedenbeck M, Yamazaki D, Katsura T (2013) Small effect of water on upper-mantle rheology based on silicon self-diffusion coefficients. Nature 498: 213-215, doi: 10.1038/nature12193

Frese K, Trommsdorff V, Kunze K (2003) Olivine [100] normal to foliation: lattice preferred orientation in prograde garnet peridotite formed at high H_2O activity, Cima di Gagnone (Central Alps). Contributions to Mineralogy and Petrology 145: 75-86, doi: 10.1007/s00410-002-0434-x

Garel F, Thoraval C, Tommasi A, Demouchy S, Davies DR (2020) Using thermo-mechanical models of subduction to constrain effective mantle viscosity. Earth and Planetary Science Letters 539: 116243, doi: 10.1016/j.epsl.2020.116243

Gouriet K and 6 coauthors (2019) Dislocation dynamics modelling of the power-law breakdown in olivine single crystals: toward a unified creep law for the upper mantle. Earth and Planetary Science Letters 506: 282-291, doi: 10.1016/j.epsl.2018.10.049

Griggs D (1967) Hydrolytic weakening of quartz and other silicates. Geophysical Journal International 14: 19-31, doi: 10.1111/j.1365-246X.1967.tb06218.x

Hansen LN, Zimmerman ME, Kohlstedt DL (2011) Grain boundary sliding in San Carlos olivine: flow law parameters and crystallographic-preferred orientation. Journal of Geophysical Research: Solid Earth 116: B08201, doi: 10.1029/2011JB008220

Hess HH (1964) Seismic anisotropy of the uppermost mantle under oceans. Nature 203: 629-631, doi: 10.1038/203629a0

Hidas K and 7 coauthors (2016) Fluid-assisted strain localization in the shallow subcontinental lithospheric mantle. Lithos 262: 636-650, doi: 10.1016/j.lithos.2016.07.038

Higgie K, Tommasi A (2012) Feedbacks between deformation and melt distribution in the crust–mantle transition zone of the Oman ophiolite. Earth and Planetary Science Letters 359-360: 61-72, doi: 10.1016/j.epsl.2012.10.003

Hirth G, Kohlstedt D (2003) Rheology of the upper mantle and the mantle wedge: a view from the experimentalists. In: Eiler J (ed) Inside the Subduction Factory. American Geophysical Union, Washington DC, pp 83-105, doi: 10.1029/138GM06

Holtzman BK and 5 coauthors (2003) Melt segregation and strain partitioning: implications for the seismic anisotropy and mantle flow. Science 301: 1227-1230, doi: 10.1126/science.1087132

Jollands MC, Dohmen, R, Padrón-Navarta, JA (2023) Hide and seek: trace element incorporation and diffusion in olivine. Elements 19: XXX-XXX

Jung H, Karato S-I (2001) Water-induced fabric transitions in olivine. Science 293: 1460-1463, doi: 10.1126/science.1062235

Kohlstedt DL (2006) The role of water in high-temperature rock deformation. Reviews in Mineralogy and Geochemistry 62: 377-396, doi: 10.2138/rmg.2006.62.16

Mainprice D, Tommasi A, Couvy H, Cordier P, Frost DJ (2005) Pressure sensitivity of olivine slip systems and seismic anisotropy of Earth's upper mantle. Nature 433: 731-733, doi: 10.1038/nature03266

Miyazaki T, Sueyoshi K, Hiraga T (2013) Olivine crystals align during diffusion creep of Earth's upper mantle. Nature 502: 321-326, doi: 10.1038/nature12570

Nakamura A, Schmalzried H (1983) On the nonstoichiometry and point defects of olivine. Physics and Chemistry of Minerals 10: 27-37, doi: 10.1007/BF01204323

Ohuchi T and 6 coauthors (2015) Dislocation-accommodated grain boundary sliding as the major deformation mechanism of olivine in the Earth's upper mantle. Science Advances 1: e1500360, doi: 10.1126/sciadv.1500360

Tielke JA, Zimmerman ME, Kohlstedt DL (2017) Hydrolytic weakening in olivine single crystals. Journal of Geophysical Research: Solid Earth 122: 3465-3479, doi: 10.1002/2017JB014004

Tommasi A, Vauchez A (2015) Heterogeneity and anisotropy in the lithospheric mantle. Tectonophysics 661: 11-37, doi: 10.1016/j.tecto.2015.07.026

Wang Q (2016) Homologous temperature of olivine: implications for creep of the upper mantle and fabric transitions in olivine. Science China Earth Sciences 59: 1138-1156, doi: 10.1007/s11430-016-5310-z

Yao Z, Qin K, Wang Q, Xue S (2019) Weak b-type olivine fabric induced by fast compaction of crystal mush in a crustal magma reservoir. Journal of Geophysical Research: Solid Earth 124: 3530-3556, doi: 10.1029/2018JB016728

Figures & Figure Captions

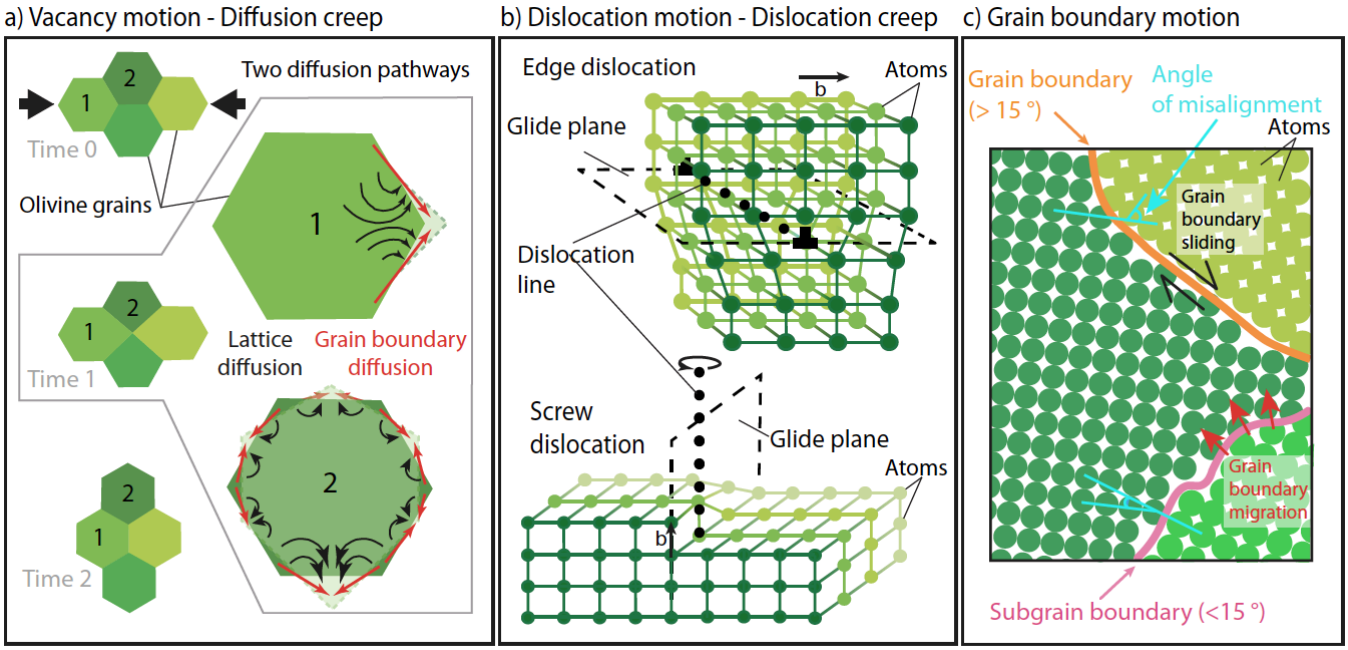

FIGURE 1. Defects in olivine. **(A)** Diffusion creep by both Si diffusion within the crystalline lattice (rate controlled by vacancy self-diffusion and concentration) and along grain boundaries. **(B)** Dislocation creep: representation of an edge dislocation with the Burgers vector ***b*** along a glide plane and a screw dislocation. Dislocation climb is not shown. **(C)** Grain boundary motion: sliding and migration of a grain boundary (misorientation/misalignment between the two crystalline lattices > 15°) and a subgrain boundary (misorientation < 15°).

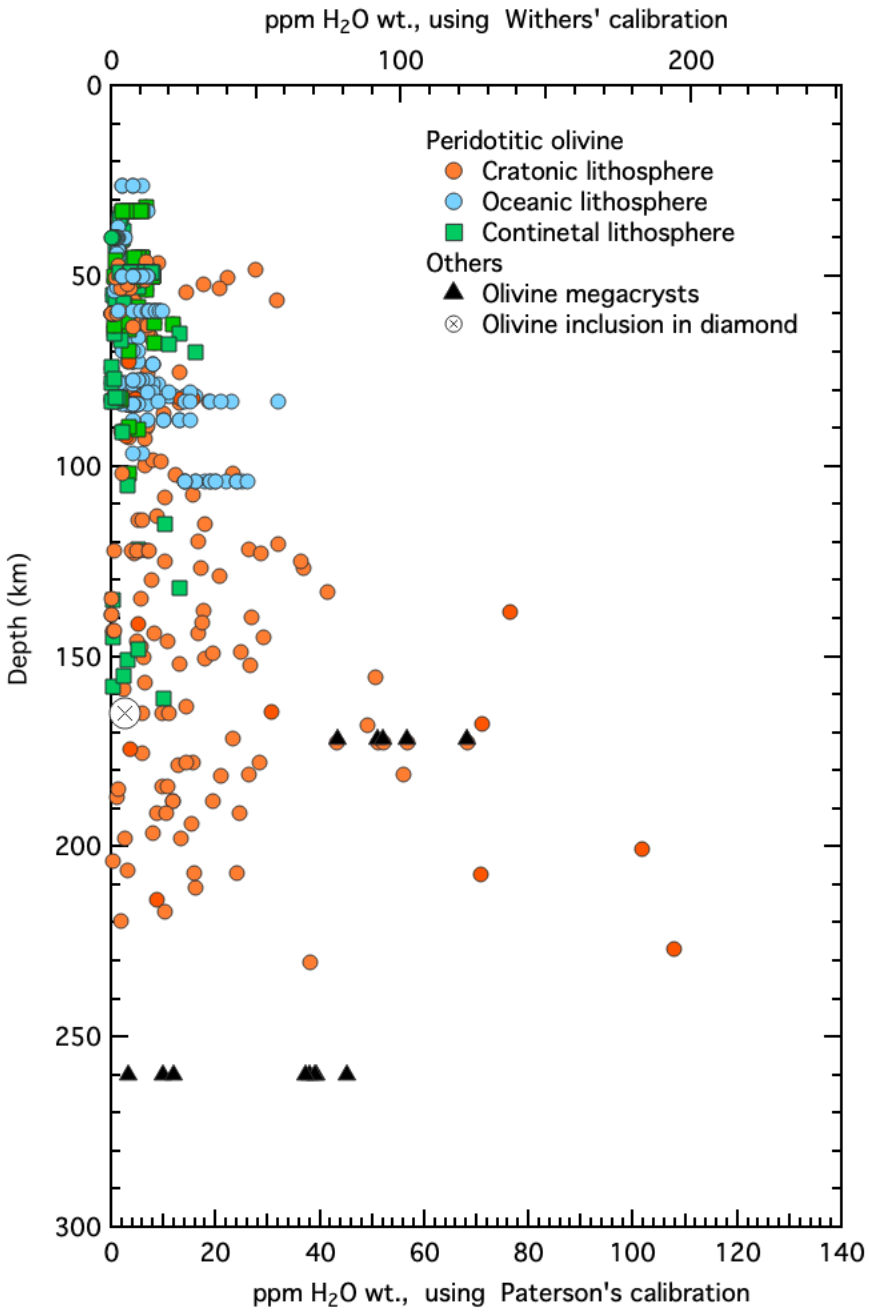

FIGURE 2. Hydrogen concentrations in olivine (in ppm wt H_2O) as a function of depth for different geological contexts. UPDATED COMPILATION BASED ON DEMOUCHY AND BOLFAN-CASANOVA (2016). Data source and methodology are provided in the online supplements.

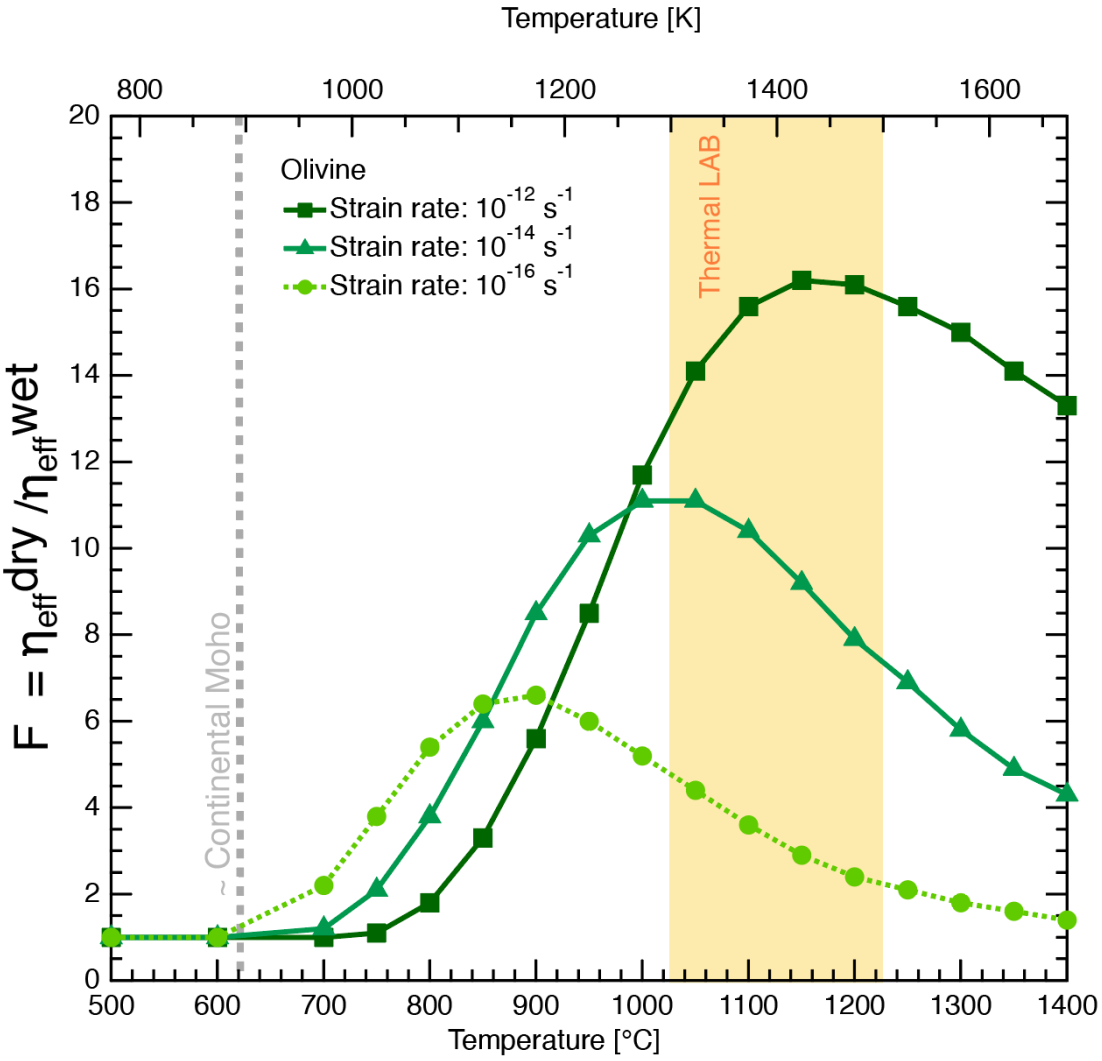

FIGURE 3. Viscosity contrast (F) defined as the ratio between the effective viscosity (stress at fixed strain rate) of a "dry" olivine and olivine containing 10 ppm H_2O by weight, for a large range of temperatures and three strain rates relevant for the upper mantle. A range of the thermal lithosphere–asthenosphere boundary (LAB) is indicated for an oceanic plate of various ages (e.g., Garel et al. 2020). The calculation is based on experimental data on olivine single crystals by TIELKE ET AL. (2017) and the flow laws reported in this study. See online supplements for methodology.

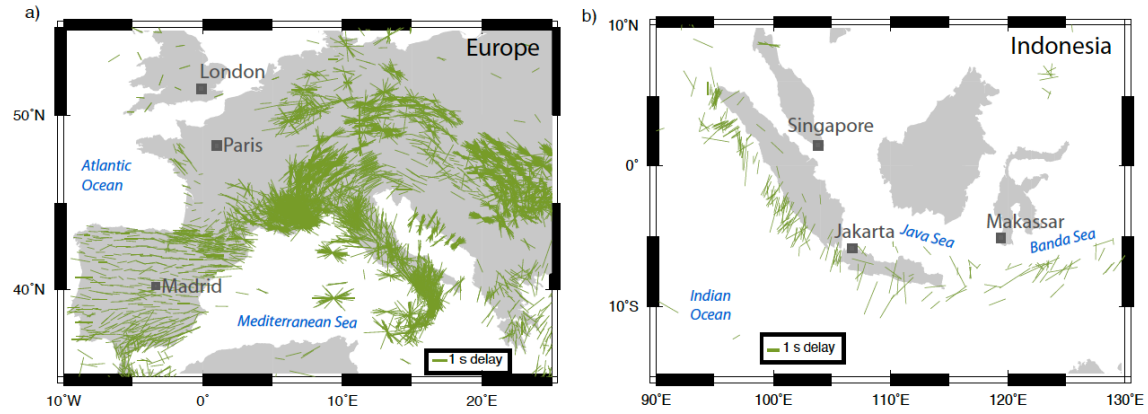

FIGURE 4. Extractions of the global teleseismic S-wave anisotropy (splitting) database (Barruol et al. 2009, see online supplements) illustrating S-wave splitting patterns at the plate scale. Teleseismic S-wave splitting is integrated along vertical paths between the core–mantle boundary and the station, with a maximum contribution from the upper mantle. The bar orientation indicates the polarization direction of the fast quasi-shear wave, and the bar length shows the delay time between the fast and slow arrivals. **(A)** Western Europe as an example of a continental plate. Note the parallelism between fast polarization directions and the strike of orogenic belts. **(B)** Indonesia as an example of a subduction zone (Indo–Australia Plate plunging northward below the Sunda Plate). Note the coexistence of dominant trench-normal fast polarization directions (consistent with corner flow model) and trench-parallel ones; this change in seismic anisotropy may result from a change in olivine CPO due to hydrogen incorporation, a preferred orientation of hydrous minerals in the wedge, or a change in flow direction. For the references for the plotted splitting data, see http://splitting.gm.univ-montp2.fr/DB/public/splittingDB_ref.txt.

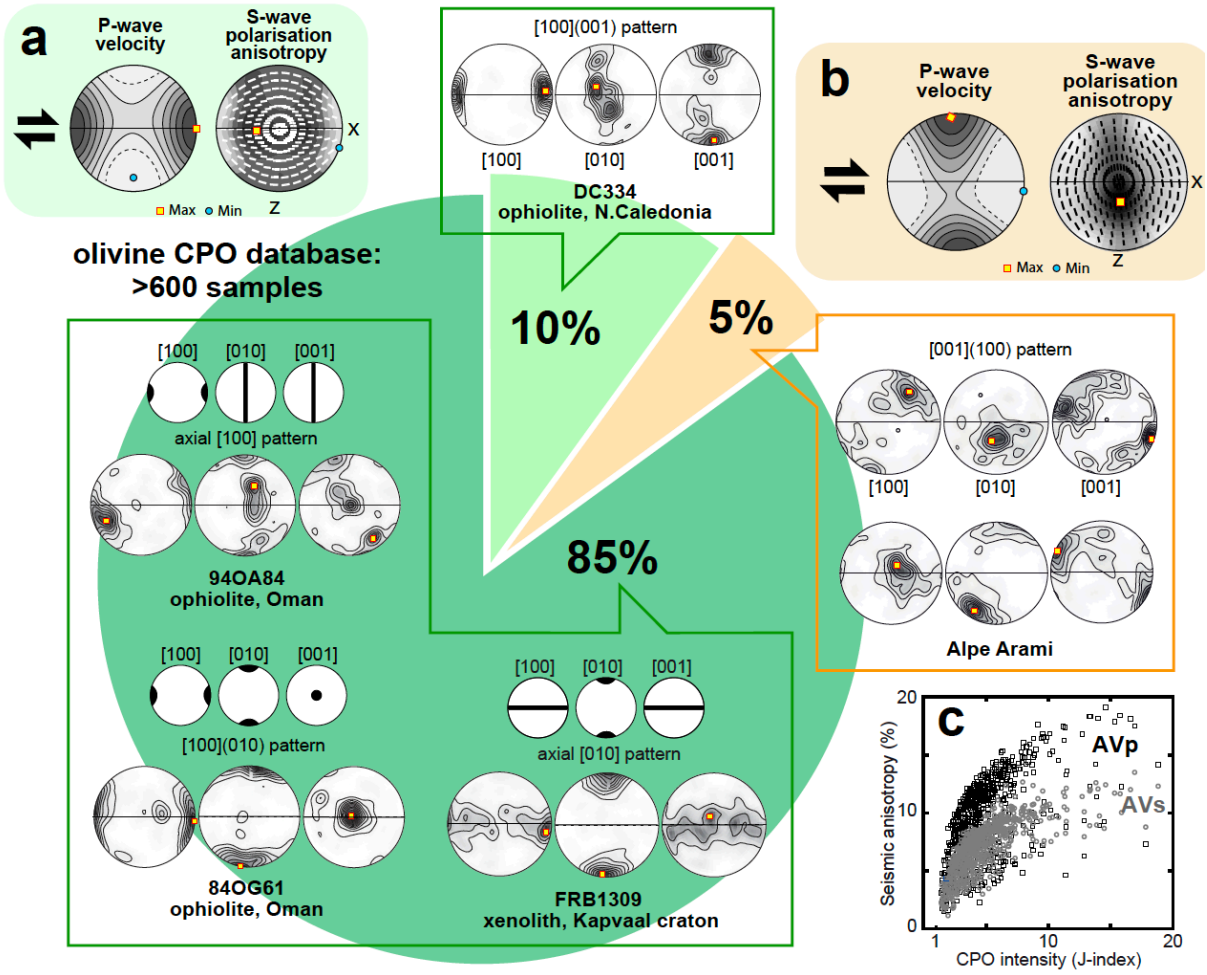

FIGURE 5. Pie chart showing the repartition of olivine CPO and seismic anisotropy patterns from the database of the Géosciences Montpellier EBSD facility, composed of > 600 peridotites including both peridotite massifs and peridotite xenoliths (Tommasi and Vauchez 2015). Olivine CPO and seismic anisotropy are displayed as pole figures, which are a stereographic representation of the orientation of lines and planes in 3D space. In all pole figures, the line marks the flow plane (Z is normal to the flow plane) and the flow direction (X) is E–W. Olivine CPO pole figures present the orientation of the three main crystallographic axes ([100], [010], and [001]) relative to the structural reference frame (here the flow plane and direction). Seismic anisotropy pole figures present the variation of P-wave velocity and the difference in velocity between the fast and slow quasi-S waves as greyscale colors. The polarization orientation of the fast quasi-S waves is indicated by white or black line segments for different propagation directions relative to the structural reference frame. **(A)** Typical seismic anisotropy pattern for olivine CPO formed by dominant [100] glide (green sections). **(B)** Typical seismic anisotropy pattern for olivine CPO formed by dominant [001] glide (orange section). **(C)** Maximum P- and S-wave anisotropies resulting from these olivine CPOs; variations in seismic anisotropy intensity result from variations

in CPO intensity (dominant effect) and symmetry. The 85% pie piece includes three CPO types (A,D and AB) defined by Jung and Karato (2001) which produce similar seismic anisotropy patterns.

Online Supplements

1. Methodology for a unified dislocation creep flow law in Eq. 4

Creep of olivine and its maze of the flow laws: Experimental high-temperature creep of metal and ceramics is successfully described by a semi-empirical power law (e.g., Frost and Ashby, 1977),

$$\dot{\varepsilon}_{high\ temperature} = \mathrm{A}'\, d^{-m}\sigma^{n}\exp\left(\frac{-E+\mathrm{PV}}{RT}\right) \qquad \text{eq. S1}$$

where T is the absolute temperature in Kelvin, A' is a material parameter, d the grain size and m its exponent, σ is the differential stress (usually in MPa), n the stress exponent, E the activation energy, R the gas constant, P the pressure and V the activation volume. This formalism was very successful to fit laboratory data for creep of olivine for $T > 0.7T_{\mathrm{m}}$ at both 1 atm and moderate confining pressure (e.g., 0.3 GPa, see for example Bai and Kohlstedt, 1992a; Mei and Kohlstedt, 2000; Faul et al., 2011, see Hirth and Kohlstedt, 2003; or Kohlstedt, 2006 for review articles). The effect of many additional parameters can be implemented in this power flow law, such as water fugacity f_{H_2O} as shown in Eq 2. in the main text (see also Bai and Kohlstedt, 1992b, 1993). Here, f_{H_2O} is a proxy for the concentration of hydrogen incorporated into the olivine lattice under saturation conditions (at high pressure and high temperature, see Kohlstedt et al., 1996 for the original solubility law, and Férot and Bolfan-Casanova, 2012 for the most recent study). Other extensive parameters impacting creep of olivine are the redox-state, oxygen fugacity f_{O_2} (e.g., Bai and Kohlstedt, 1992a; Cline et al., 2018), iron content (e.g., Zhao et al., 2009; 2018), titanium content (e.g., Faul et al., 2016), silica activity (e.g., Bai and Kohlstedt, 1992a), basaltic melt fraction (e.g., Holtzman et al. 2003a, 2003b; Zimmerman and Kohlstedt, 2004) or even fraction of molten metals (e.g., Hustoft et al., 2006).

A more comprehensive power flow law may be defined as follows (without pressure-dependency) (Kohlstedt et al., 2000):

$$\dot{\varepsilon}_{high\ temperature} = \mathrm{A}'' d^{-m}\ f_{H_2O}{}^{r}\ f_{O_2}{}^{s} a_{SiO2}^{w}\ X_{impurities}^{t}\ \sigma^{n}\ \exp(\alpha\varphi)\ \exp\left(\frac{-E}{RT}\right) \qquad \text{eq. S2}$$

where *A'* is a material parameter, *m, r, s, w,* and *t* are exponents for each additional parameter, determined by data fitting, φ is the volume fraction of melt. The α parameter defines the dependence of strain rate on melt fraction (also called the melt fraction factor), which is a function of *T*, *P*, and melt chemical composition and other hidden parameters such as the wetting properties of the studied melt or the grain boundary contiguity (e.g., Takei, 1998). This formulation has the advantage to be versatile, but also holds several disadvantages: (1) it requires a massive number of experiments to obtain a reliable fit to the data; (2) one must assume that a single creep mechanism accommodates most deformation in all actively deformed zones, and (3) it implies that the dominant mechanisms at laboratory strain rates remain the same at the much (ten orders of magnitude) slower strain rates relevant for geodynamics, which is a critical assumption.

The above power law formalism generally satisfies simple systems at high temperature, but at the stresses needed to deform olivine below 0.7*Tm* at laboratory strain rates (10^{-6}-10^{-4} s^{-1}), the power law breaks down and an exponential law formalism is generally used to fit the data (e.g., Evans and Goetze, 1979).

$$\dot{\varepsilon}_{low\ temperaure} = \mathrm{B}\exp\left(\frac{-E}{RT}\left(1-\left(\frac{\sigma}{\sigma_{Peierls}}\right)^{\mathrm{p}}\right)^{\mathrm{q}}\right) \qquad \text{eq. S3}$$

where *B* is a material parameter (different than A, A' or A''), σ_P is the Peierls' stress (often in GPa, as for σ in this formulation). $\sigma_{Peierls}$ originally represents the 'lattice friction', i.e., the stress needed to move a dislocation within a plane of atoms at 0 K as defined by Peierls (1940) and modified by Nabarro (1947), but it is used here as a proxy of the general resistance to dislocation glide at 0 K. The values of *p* and *q* are determined empirically and are generally bracketed by $0 \leq p \leq 1$ and $1 \leq q \leq 2$ (Frost and Ashby, 1982; Kocks *et al.*, 1975, p. 142). Although the *p* and *q* exponents are fundamental in this flow law, they are usually fixed prior to data fitting (Evans and Goetze, 1979; Raterron et al. 2004 ; Katayama and Karato , 2008 ; Mei et al., 2010, Demouchy et al., 2013; Hansen et al., 2019).

It is traditionally proposed that the transition between the exponential and power law behaviors is associated with the onset of dislocation climb (Evans and Goetze, 1979). The impact of dislocation climb is difficult to extract and quantify in laboratory-based experiments, but it may be easily controlled in numerical modelling approach based on 2.5-dimensional dislocation dynamics simulations. This question was expressely targeted in three recent studies (Boioli et al., 2015a, 2015b; Gouriet et al., 2019), which analyzed the high temperature and low temperature deformation of single crystals of iron-free and hydrogen-free olivine. Comparison between these studies showed continuity between the deformation two regimes (high temperature and low temperature), implying that the use of two separated semi-empirical rheological laws (Eq. S1 and Eq. S3) to describe the creep of olivine was only motivated by convenience and is in fact not imposed by theoretical needs. The low and high temperature behaviors can then be unified into a single flow law for dislocation creep in olivine, directedly calculated for temperatures and strain rates relevant for the Earth upper mantle (800–1700 K and stress between 50 and 500 MPa, see Gouriet et al. 2019):

$$\dot{\varepsilon}_{unified\ dislocation\ creep} = \mathrm{C}\left(\frac{\sigma}{\mu}\right)^{\mathrm{n}} \exp\left(\frac{-E}{RT}\left(1-\left(\frac{\sigma}{\sigma_{Peierls}}\right)^{\mathrm{p}}\right)^{\mathrm{q}}\right) \qquad \text{eq. S4}$$

where *C* is a material parameter (different than A, A', A'' or B), and μ is shear modulus in GPa. The numerical results from Gouriet et al. (2019) yield:

$$\dot{\varepsilon}_{unified\ dislocation\ creep} = 1.7\times10^{16}\left(\frac{\sigma}{\mu}\right)^{2.95} \exp\left(\frac{-460\times10^{3}}{RT}\left(1-\left(\frac{\sigma(MPa)}{2000(MPa)}\right)^{1.52}\right)^{2}\right) \quad \text{eq. S5}$$

This unified flow law reproduces well the long-term upper mantle viscoelastoplastic behavior and includes the power law breakdown, which occurs for stresses higher than 200 MPa. Comparison of the strength envelope for a continental plate predicted using this unified flow with typical set of (power and exponential) flow laws used to model olivine ductile deformation is shown in Figure S1. As explained in the main text, this unified formulation yields a non-linear behavior, with the strongest non-linearity (stress dependence) at low temperature, consistent with observations in nature, where the strongest strain localization is associated with low-temperature/high stresses plastic deformation (in olivine rich-rocks, but also in crustal rocks). We emphasize that the exponential form is not strictly required from theoretical reasons, and for implementation in geodynamical models where stress should be

expressed as a function of strain rate and temperature, other mathematical formulations may be proposed to fit the dislocation dynamics modelling data such as a hyperbolic tangent (tanh) (e.g., Garel et al., 2020; Garel and Thoraval, 2021).

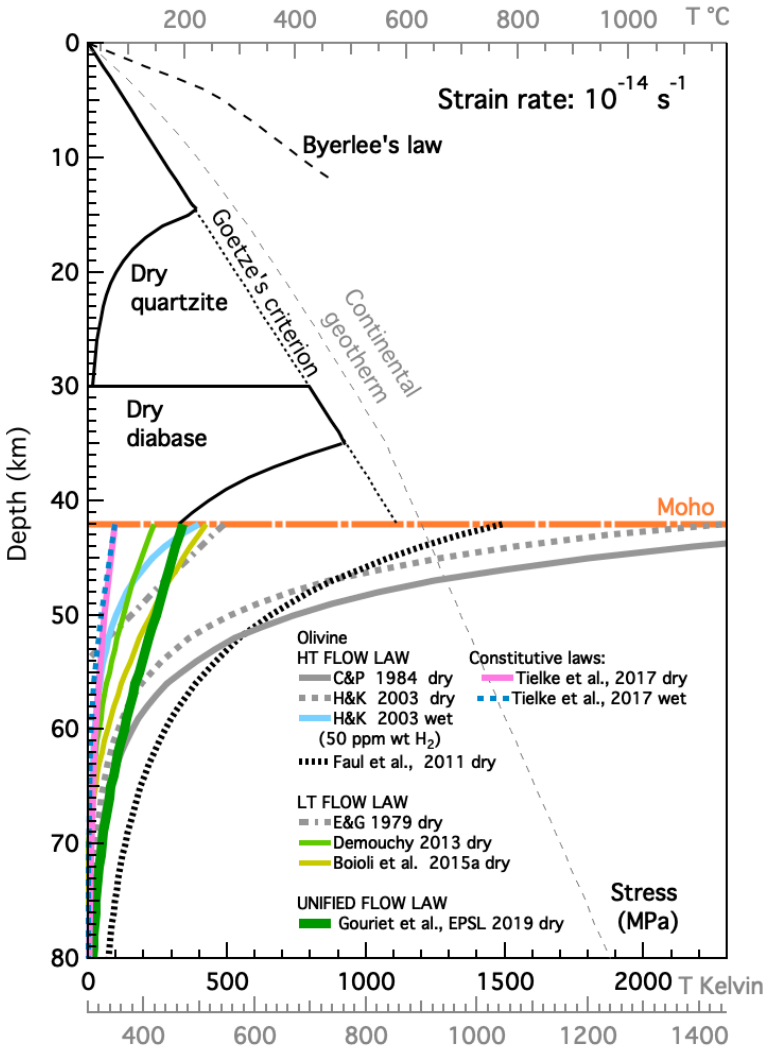

Figure S1. Strength envelope model for a continental lithosphere deforming at a constant strain rate of 10^{-14} s^{-1}. The geotherm is plotted in grey. Frictional sliding law is from Byerlee (1979). Goetze's criterion was calculated with a density of 2700 $kg.m^{-3}$ for the crust. Flow laws for dry quartzite (Gleason and Tullis, 1994) and dry diabase (Mackwell et al., 1998) are used for the upper and lower crust, respectively. Creep of olivine is shown for a variety of flow laws: low-temperature (LT) flow law from Boioli et al. (2015b); Demouchy et al., (2013), Evans and Goezte (1978) as well as 'dry' and 'wet' high-temperature (HT) flow laws from Hirth and Kohlstedt (2003), 'dry' HT flow laws from Faul et al., (2011) and Chopra and Paterson (1984), and the unified flow law from Gouriet et al. (2019). We also added the flow laws (dry and wet) from Tielke et al. (2017), which are further discussed in the online supplement section 3.

1. Nakamura A, Schmalzried H (1983) On the nonstoichiometry and point defects of olivine. Physics and Chemistry of Minerals 10: 27–37

References

Bai Q, Kohlstedt, DL (1992a) High-temperature creep of olivine single crystals III. Mechanical results for unbuffered samples and creep mechanisms. Philosophical Magazine A. 66:1149–1181

Bai Q, Kohlstedt, DL (1992b) Substantial hydrogen solubility in olivine and implications for water storage in the mantle. Nature 35: 672–674

Bai Q, Kohlstedt, DL (1993) Effects of chemical environment on the solubility and incorporation mechanism for hydrogen in olivine. Physics and Chemistry of Minerals 19:460–471.

Bai Q, Mackwell SJ, Kohlstedt DL (1991) High-temperature creep of olivine single crystals. 1. Mechanical results for buffered samples. Journal of Geophysical Research 96:2441–2463.

Boioli F, Carrez P, Cordier P, Devincre B, Marquille M (2015) Modeling the creep properties of olivine by 2.5-dimensional dislocation dynamics simulations. Physics Review B 92 :014115.

Boioli F, Tommasi A, Cordier P, Demouchy S, Mussi A (2015) Low steady-state stresses in the cold lithospheric mantle inferred from dislocation dynamics models of dislocation creep in olivine. Earth and Planetary Science Letters 432:232–242.

Byerlee JD, Brace WF (1968) Stick slip stable sliding and earthquakes - effect of rock type pressure strain rate and stiffness. Journal of Geophysical Research 73:6031

Chopra PN, Paterson MS (1984) The role of water in the deformation of dunite. Journal of Geophysical Research. 89:7861-7876

Cline CJ, Faul UH, David EC, Berry AJ, Jackson I (2018) Redox-influenced seismic properties of upper-mantle olivine. Nature 555:355–358

Demouchy S, Tommasi A, Ballaran TB, Cordier P (2013) Low strength of Earth's uppermost mantle inferred from tri-axial deformation experiments on dry olivine crystals. Physics of the Earth and Planetary Interiors 220:37–49

Evans B, Goetze C (1979) The temperature variation of hardness of olivine and its implication for polycrystalline yield stress. Journal of Geophysical Research 84:5505–5524

Faul UH, Cline CJ II, David EC, Berry AJ, Jackson I (2016) Titanium-hydroxyl defect-controlled rheology of the Earth's upper mantle. Earth and Planetary Science Letters 452:227–237.

Faul UH, Gerald JF, Farla RJM, Ahlefeldt R, Jackson, I (2011) Dislocation creep of fine-grained olivine. Journal of Geophysical Research 116, doi: 10.0129–2009JB007174

Férot A, Bolfan-Casanova N (2012) Water storage capacity in olivine and pyroxene to 14 GPa: Implications for the water content of the Earth's upper mantle and nature of seismic discontinuities. Earth and Planetary Science Letters 349-350:218–230.

Frost HJ, Ashby MF (1982). Deformation mechanism maps: the plasticity and creep of metals and ceramics. Pergamon press, oxford.

Garel F, Thoraval C (2021) Lithosphere as a constant-velocity plate: Chasing a dynamical LAB in a homogeneous mantle material. Physics of the Earth and Planetary Interiors 316: 106710.

Garel F, Thoraval C, Tommasi A, Demouchy S, Davies R (2020) Using thermo-mechanical models of subduction to constrain effective mantle rheology. Earth and Planetary Science Letters 539: 116243

Gleason GC, Tullis J, (1993) Improving flow laws and piezometers for quartz and feldspar aggregates. Geophysical Research Letters 20:2111-2114

Gouriet K, Cordier P, Garel F, Thoraval C, Demouchy S, Tommasi A, Carrez P (2019) Dislocation dynamics modelling of the power-law breakdown in olivine single crystals: Toward a unified creep law for the upper mantle. Earth and Planetary Science Letters 506: 282–291

Hansen LN, Kumamoto KM, Thom CA, Wallis D, Durham WB, Goldsby DL, Breithaupt T, Meyers, CD, Kohlstedt DL (2019) Low-temperature plasticity in olivine: Grain size, strain hardening, and the strength of the lithosphere. Journal of Geophysical Research: Solid Earth, 124,:5427–5449

Hirth G, Kohlstedt DL (2003) Rheology of the upper mantle and the mantle wedge: a view from the experimentalists, in: Eiler, J. (Ed.), Inside The Subduction Factory. American Geophysical Union, Washington D.C., pp. 83–105.
Holtzman BK, Groebner NJ, Zimmerman ME, Ginsberg SB, Kohlstedt D (2003) Stress-driven melt segregation in partially molten rocks. Geochemistry, Geophysics and Geosystems 4, doi:10.1029–2001GC000258.
Holtzman BK, Kohlstedt DL, Zimmerman ME, Heidelbach F, Hiraga T, Hustoft J (2003) Melt segregation and strain partitioning: Implications for the seismic anisotropy and mantle flow. Science 301:1227–1230
Hustoft JW, Kohlstedt DL (2006) Melt-silicate segregation in deforming dunitic rock. Geochemistry, Geophysics and Geosystems https://doi.org/10.1029/2005GC001048.
Katayama I, Karato SI (2008) Low-temperature, high-stress deformation of olivine under water-saturated conditions. Physics of the Earth and Planetary Interiors 168 (3-4): 125-133
Kocks UF, Argon AS, Ashby MF (1975) 4. Thermal activation, in: Kocks, U.F., Argon, A.S., Ashby, M.F. (Eds.), Thermodynamics and Kinetics of Slip. Pergamon Press, pp. 110–271
Kohlstedt DL (2006) The Role of Water in High-Temperature Rock Deformation. Reviews in Mineralogy and Geochemistry 62:377–396
Kohlstedt DL, Bai Q, Wang Z-C, Mei S (2000) Chapter 1. Rheology of Partially Molten Rocks inPhysics and chemistry of Partially molten rock, Ed. N. Bagdassarov, D. Laporte; A. Bruce Thompson, Kulwer academic publishing.3-28
Kohlstedt DL, Keppler H, Rubie DC (1996) Solubility of water in the α, β and γ phases of $(Mg,Fe)_2SiO_4$. Contribution to Mineralogy and Petrology 123: 345–357
Mackwell SJ, Zimmerman ME, Kohlstedt DL (1998) High-temperature deformation of dry diabase with application to tectonics on Venus. Journal of Geophysical Research 103:975-984
Mei S, Kohlstedt DL (2000) Influence of water on plastic deformation of olivine aggregates 2. Dislocation creep regime. Journal of Geophysical Research 105: 21471–21481.
Mei S. Suzuki A, Kohlstedt DL, Dixon NA, Durham WB (2010). Experimental constraints on the strength of the lithospheric mantle. Journal of Geophysical Research 115, doi:10.1029–2009–JB006873. doi:10.1029/2009/JB006873
Nabarro FRN (1947) Dislocations in a simple cubic lattice. Proceeding of the Physical Society 59:256–272.
Peierls RE (1940) The size of a dislocation. Proceeding of the Physical Society 52:34–37.
Raterron P, Wu,Y, Weidner DJ, Chen J (2004) Low-temperature olivine rheology at high pressure. Physics of the Earth and Planetary Interiors 145:149–159.
Takei Y, (1998) Constitutive mechanical relations of solid-liquid composites in terms of grain-boundary contiguity. Journal of Geophysical Research 1093:18183–18203.
Zhao YH, Zimmerman ME, Kohlstedt DL (2018). Effect of iron content on the creep behavior of Olivine_ 2. Hydrous conditions. Physics of the Earth and Planetary Interiors 278:26–33.
Zhao YH, Zimmerman ME, Kohlstedt DL (2009) Effect of iron content on the creep behavior of olivine: 1. Anhydrous conditions. Earth and Planetary Science Letters 287:229–240.
Zimmerman ME, Kohlstedt DL (2004) Rheological properties of partially molten lherzolite. Journal Petrology 2:275–298.

2. Data source and methodology for Figure 2

Figure 2 reported hydrogen concentrations in olivine from peridotites obtained by Fourier transform infrared spectroscopy (FTIR). This analytical method is not an absolute

method of quantification; measured absorbances need to be calibrated to obtain hydrogen concentrations in nominally anhydrous minerals (Demouchy and Bolfan-Casanova, 2016; Rossman, 2006). Two different types of calibrations are used to build Fig. 2: (i) the empirical frequency-dependent calibration of Paterson (1982) for unpolarized infrared data and (ii) a mineral-dependent calibration (Withers et al., 2012 for olivine only). These calibrations result in a detection limit of about 1 ppm wt H_2O for a 1-mm-thick olivine sample (e.g., Denis et al., 2015). The estimated error from the empirical calibration in the resulting H concentration in olivine is around 30 % (Paterson, 1982); it is lower (10-15 %) for the olivine calibration from Withers et al. (2012). The frequency-dependent calibration of Paterson (1982) is given as

$$C_{OH} = \frac{\chi i}{150\zeta} \int \frac{\mathrm{k}(\upsilon)}{3780-\upsilon} d\upsilon. \qquad \text{eq.7}$$

where the following mineral specific factors χ_i (Paterson, 1982) were used based on the chemical composition in major elements of the mineral *i* (see method of calculation in Demouchy and Bolfan-Casanova, 2016): χ_{ol} = 2663 ppm wt H_2O for $Fo_{89.2}$, ζ is the orientation factor, which equals 1/3 for unpolarized infrared analyses (Paterson, 1982). The absorption coefficient k(υ) is a function of the wavenumber υ. Integration of the spectrum was performed between 3620 and 2900 cm^{-1} for olivine. Multiplying the average concentrations obtained by unpolarized infrared by a factor three yields estimates comparable to the sum of concentrations obtained by polarized infrared measurements along the three main crystallographic axes (see Fig. S1 in Férot and Bolfan-Casanova, 2012). Note that the calibration of Bell et al., (2003) was found to overestimate hydrogen concentrations in olivine (see Withers et al., 2012 for details). This calibration was originally used in several articles for the compilation, these hydrogen concentrations were then converted for comparison purpose in Fig. 2. One question remains regarding the current database of hydrogen distribution in mantle olivine. Hydrogen diffusivities quantified using laboratory measurements yield fast diffusion coefficients (e.g., Mackwell and Kohlstedt, 1990; Demouchy and Mackwell, 2006), implying a very elusive storage of hydrogen at depth with time. These data are somehow incompatible with a persistent residual and non-negligible hydrogen content in peridotitic olivine (Fig. 2), which increases with depth. The atomic-scale storage mechanism responsible for the discrepancy is not yet fully solved despite several attempts (e.g., Thoraval et al., 2018: Demouchy et al., 2016: Padron-Navarta and Hermann, 2017). This question requires further experimental studies as well as numerical investigation.

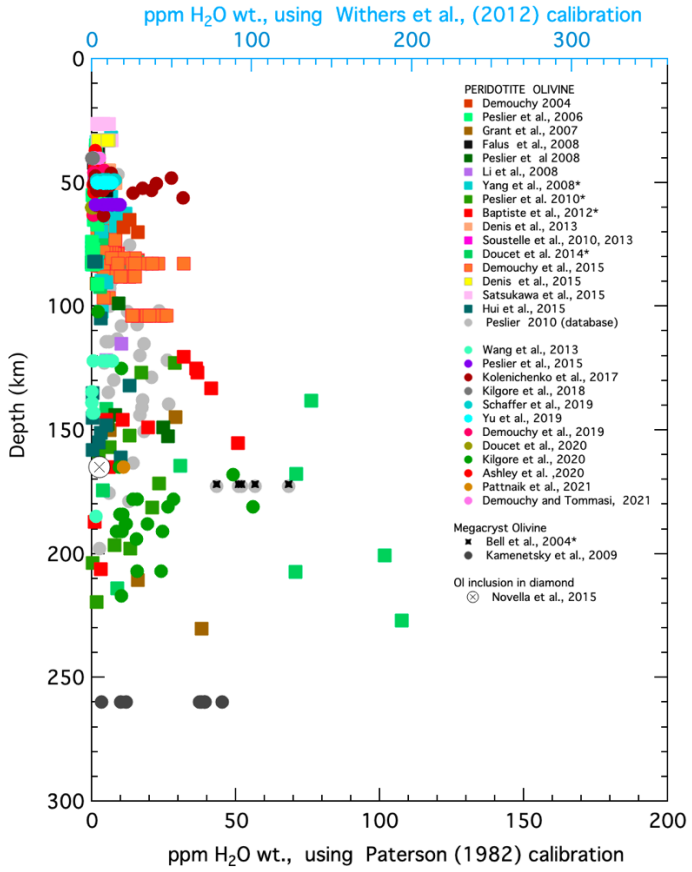

Figure S2. Hydrogen concentrations in olivine (in ppm wt H_2O) as a function of depth. The database is a compilation from Baptiste et al., 2012; Bell et al., 2004; Demouchy and Bolfan-Casanova 2016; Demouchy, 2004; Denis et al., 2013, 2015; Doucet et al., 2014; Falus et al., 2007; Grant et al., 2007; Hui et al., 2015; Kamenetsky et al., 2009, Li et al., 2008; Novella et al., 2015; Peslier, 2010; Peslier, et al., 2007, 2008; 2010; Satsukawa et al., 2015; Soustelle et al., 2010, 2013; Yang et al., 2008), updated with the most recent studies (Ashley et al., 2020; Demouchy and Tommasi, 2021; Demouchy et al., 2019; Doucet et al., 2020; Kilgore et al., 2018, 2020; Kolenichenko et al., 2017; Pattnaik et al., 2021; Peslier et al., 2015; Schaeffer et al., 2019, Wang et al., 2013 ; Yu et al., 2019).

References

Ashley AW, Bizimis M, Peslier AH, Jackson M (2020) Metasomatism and Hydration of the Oceanic Lithosphere: a Case Study of Peridotite Xenoliths from Samoa. Journal of Petrology 61:1–29.

Baptiste V, Tommasi A, Vauchez A, Demouchy S, Rudnick RL (2015) Deformation, hydration, and anisotropy of the lithospheric mantle in an active rift: Constraints from mantle xenoliths from the North Tanzanian Divergence of the East African Rift. Tectonophysics 639: 34–55.

Bell DR, Rossman GR, Maldener J, Endisch D, Rauch,F (2003) Hydroxide in olivine: a quantitative determination of the absolute amount and calibration of the IR spectrum. Journal of Geophysical Research 108

Bell DR, Rossman, GR, Moore RO (2004) Abondance and partitioning of OH in a high-pressure magmatic system: Megacrysts from the Monastery kimberlite, South Africa. Journal of Petrology 45: 1539–1564

Demouchy S (2004) Thermodynamics and kinetics of hydrogen incorporation in olivine and wadsleyite. Bayreuth, Bayreuth

Demouch ., Bolfan-Casanova N (2016) Distribution and transport of hydrogen in the lithospheric mantle: A review. Lithos 240-243:402–425

Demouchy S, Mackwell, S (2006) Mechanisms of hydrogen incorporation and diffusion in iron-bearing olivine. Physics and Chemistry of Minerals 33:347–355

Demouchy S, Thoraval C, Bolfan-Casanova N, Manthilake G (2016) Diffusivity of hydrogen in iron-bearing olivine at 3 GPa. Physics of the Earth and Planetary Interiors 260:1–13.

Demouchy S, Tommasi A (2021) From dry to damp and stiff mantle lithosphere by reactive melt percolation atop the Hawaii plume. Earth and Planary Science Letters 574:117159.

Demouchy S, Tommasi A, Ionov D, Higgie K, Carlson RW (2019) Microstructures, Water Contents, and Seismic Properties of the Mantle Lithosphere beneath the Northern limit of the Hangay Dome, Mongolia. Geochem. Geophys. Geosyst. 2018GC007931.

Denis C, Demouchy S, Shaw C (2013) Evidence of dehydration in peridotites from Eifel Volcanic Field and estimates of magma ascent rates. Journal of Volcanology and Geothermal Research 258: 85–99

Denis CMM, Alard O, Demouchy S (2015) Water content and hydrogen behaviour during metasomatism in the uppermost mantle beneath Ray Pic volcano (Massif Central, France). Lithos 236-237:256–274.

Doucet LS, Peslier AH, Ionov DA. Brandon AD, Golovin AV, Goncharov AG, Ashchepkov IV (2014) High water contents in the Siberian cratonic mantle linked to metasomatism: an FTIR study of Udachnaya peridotite xenoliths. Geochimica et Cosmochimica Acta, 1–75.

Doucet LS, Xu Y, Klaessens D, Hui H, Ionov DA, Mattielli AN (2020) Decoupled water and iron enrichments in the cratonic mantle: A study on peridotite xenoliths from Tok, SE Siberian Craton, American Mineralogist 105(6).

Falus G. Tommasi A, Ingrin J, Szabo C (2008) Deformation and seismic anisotropy of the lithospheric mantle in the Southeastern Carpathians inferred from the study of mantle xenoliths. Earth and Planetary Science Letters 272:50–64

Férot A, Bolfan-Casanova N (2012) Water storage capacity in olivine and pyroxene to 14 GPa: Implications for the water content of the Earth's upper mantle and nature of seismic discontinuities. Earth and Planetary Science Letters 349-350:218–230.

Grant K, Ingrin J, Lorand JP, Dumas P (2007) Water partitioning between mantle minerals from peridotite xenoliths. Contribution to Mineralogy and Petrology 154:15–34.

Hui H, Peslier AH, Rudnick RL, Simonetti A, Neal CR (2015) Plume-cratonic lithosphere interaction recorded by water and other trace elements in peridotite xenoliths from the Labait volcano, Tanzania. Geochemistry, Geophysics, Geosystems 16:1687–1710.

Kamenetsky VS, Kamenetsky MB, Sobole AV, Golovin AV, Demouchy S, Faure K, Sharygin VV, Kuzmin DV (2009) Olivine in the Udachnaya-East Kimberlite (Yakutia, Russia): Types, compositions and origins. Journal of Petrology 49:823–839.

Kilgore ML, Peslier AH, Brandon AD, Lamb W (2018); Water and Oxygen Fugacity in the Lithospheric Mantle Wedge Beneath the Northern Canadian Cordillera (Alligator Lake). Geochemistry, Geophysics, Geosystems 19 (10). DOI: 10.1029/2018GC007700

Kilgore ML, Peslier AH, Brandon AD, Schaffer L, Morris RV, Graff TG, Agresti DG, O'Reilly SY, Griffin WL, Pearson G, Gangi K, Shaulis BJ (2020) Metasomatic control of hydrogen contents in the layered cratonic mantle lithosphere sampled by Lac de Gras xenoliths in the central Slave craton, Canada. Geochimica et Cosmochimica Acta, 286:29-53.

Kolesnichenko MV, Zedgenizov DA, Litasov KD, Safonova IY, Ragozin AL (2017) Heterogeneous distribution of water in the mantle beneath the central Siberian Craton: Implications from the Udachnaya Kimberlite Pipe, Gondwana Research, 47:249-266

Li ZXA, Lee, CTA, Peslier A, Lenardic A, Mackwell SJ (2008) Water contents in mantle xenoliths from the Colorado Plateau and vicinity: implications for the mantle rheology and hydration-induced thinning of continental lithosphere. Journal of Geophysical Research 113, doi: 10.1029–2007JB005540

Mackwell SJ, Kohlstedt DL (1990) Diffusion of hydrogen in olivine: Implications for water in the mantle. Journal of Geophysical Research 95:5079–5088

Novella D, Bolfan-Casanova N, Nestola,F, Harris JW (2015) H_2O in olivine and garnet inclusions still trapped in diamonds from the Siberian craton: Implications for the water content of cratonic lithosphere peridotites. Lithos 230:180–183

Padron-Navarta, JA, Hermann, J (2017) A Subsolidus Olivine Water Solubility Equation for the Earth's Upper Mantle. Journal of Geophysical Research Solid Earth 122: 9862–9880.

Paterson MS (1982) The determination of hydroxyl by infrared absorption in quartz, silicate glasses and similar materials. Bulletin de Minéralogie 105,:20–29

Pattnaik, J, Demouchy S, Ghosh SK (2021) Hydrogen concentrations in mantle xenoliths and minerals from Wajrakarur kimberlite field, Eastern Dharwar Craton, India. Precambrian Research, 352:105982

Peslier A, Luhr JF (2006) Hydrogen loss form olivines in mantle xenoliths from Sincoe (USA) and Mexico: mafic alkalic magma ascent rate and water budget of the sub-continental lithosphere. Earth and Planetary Science Letters 242, 302–314

Peslier A, Woodland AB, Wolff,JA (2008) Fast kimberlite ascent rates estimates from hydrogen diffusion profiles in xenoliths mantle olivines from South Africa. Geochemistry Geophysics and Geosystems 72:2711–2722

Peslier AH (2010) A review of water contents of nominally anhydrous minerals in the mantles of Earth, Mars and the Moon. Journal Volcanology and Geothermal Research 197:239–258

Peslier AH, Bizimis M, Matney M (2015) Water disequilibrium in olivines from Hawaiian peridotites: Recent metasomatism, H diffusion and magma ascent rates. Geochimica et Cosmocimica Acta 1–66. doi:10.1016/j.gca.2015.01.030.

Peslier AH, Woodland AB, Bell DR, Lazarov M (2010) Olivine water contents in the continental lithosphere and the longevity of cratons. Nature 467:78–83

Rossman GR (2006) Analytical Methods for Measuring Water in Nominally Anhydrous Minerals. Reviews in Mineralogy and Geochemistry 62:1–28

Satsukawa T, Godard M, Demouchy S, Michibayashi K, Ildefonse B (2017) Chemical interactions in the subduction factory: New insights from an *in situ* trace element and hydrogen study of the Ichinomegata and Oki-Dogo mantle xenoliths (Japan) Chemical Geology, 234–267

Shaffer LA, Peslier AH, Brandon AD, Bizimis M, Gibler R, Norman M, Harvey J (2018) Effects of melting, subduction-related metasomatism, and sub-solidus equilibration on the distribution of water contents in the mantle beneath the Rio Grande Rift (USA). Geochimica et Cosmochimica Acta doi:0.1016/j.gca.2018.10.005.

Soustelle V, Tommasi A, Demouchy S, Ionov D (2010) Deformation and fluid-rock interactions in supra-subduction mantle : Microstructures and water contents in peridotite xenoliths from the Avacha volcano, Kamchatka. Journal of Petrology 51:363–394

Soustelle V, Tommasi A, Demouchy S, Franz, L (2013) Melt-rock interactions, deformation, hydration and seismic properties in the sub-arc lithospheric mantle inferred from xenoliths from seamounts near Lihir, Papua New Guinea. Tectonophysics 608:330–345

Thoraval C, Demouchy S, Padrón-Navarta JA (2019) Relative diffusivities of hydrous defects from a partially dehydrated natural olivine. Physics and Chemistry of Minerals46:1-13.

Wang Q, Xia Q-K, O'Reilly SY, Griffin WL, Beyer EE, Bruecknes HK (2013) Pressure- and stress-induced fabric transition in olivine from peridotites in the Western Gneiss Region (Norway): implications for mantle seismic anisotropy. Journal of Metamorphic Geology 31:93-111

Withers,AC, Bureau H, Raepsaet C, Hirschmann MM, (2012) Calibration of infrared spectroscopy by elastic recoil detection analysis of H in synthetic olivine. Chemical Geology 334:92–98

Yang X-Z, Xia Q-K, Deloule E, Dallai L, Fan Q-C, Feng M (2008) Water in minerals of the continental lithospheric mantle and overlying lower crust: A comparative study of peridotite and granulite xenoliths from the North China Craton. Chemical Geology 256: 33–45
Yu M, Wang Q, Yang J (2019) Fabrics and water contents of peridotites in the Neotethyan Luobusa ophiolite, southern Tibet: implications for mantle recycling in supra-subduction zones. Journal of the Geological Society 176:975-991

3. Methodology for Figure 3

Figure 3 was built using the high-temperature and low-temperature flow laws reported by Tielke et al. (2017, their figure 10). The 'wet' flow law corresponds to the equation 16 in Tielke et al. (2017) for olivine single crystals deformed in axial compression at 45° to the [100] and [001] axes, as to activate glide of dislocations with both [100] and [001] Burgers vectors. The dry high-temperature power flow is from Bai et al. (1991) and the dry low-temperature (exponential) flow law corresponds to equation 17 in Tielke et al. (2017). Note that the effect of hydrogen on the rheology of olivine is weak (well below a factor 10) at low temperatures (<1100 °C) according to this recent experimental study, confirming other experimental studies on both single crystals and polycrystalline olivine (Demouchy et al., 2012, Girard et al., 2013). First the strain rates as a function of temperature for a fixed stress of 100 MPa are calculated, then they are extrapolated to slower strain rates (10^{-16}-10^{-14} Pas) and down to a stress of 10 MPa, which is an estimated relevant for the base of the lithosphere, as illustrated in Figure S3a. Then, following the same flow laws, stresses are calculated for fixed strain rates relevant for the mantle lithosphere as shown in Figure S3b. Subsequently effective viscosities, defined as as,

$$\eta_{eff} = \frac{\sigma}{\dot{\varepsilon}} \qquad \text{eq. S6}$$

were calculated for each temperature (data points in Figure S3b) and the ratio of the two effective viscosities (wet and dry) are finally calculated and displayed in Figure 3 (in the main text).

The hydrogen concentration was not adjusted (increased nor decreased) as it already corresponds to an appropriate water content for a spinel-bearing mantle lithosphere as shown by Figure 2 in the main text (see also Demouchy and Bolfan-Casanova, 2016).

Nevertheless, the calculation above is based on experimental data obtained on olivine single-crystals only. The impact of hydrogen stored at grain boundaries on the rheological properties of coarse-grained peridotites still need to be assessed (see Demouchy et al., 2012).

We recall below the equation used for the calculation for oxygen fugacity along the Ni-NiO buffer needed for the dry power flow law from Bai et al. (1991):

$$f_{O2} = 10^{(12.78-2.5073\times(10000/(T))} - (1.1 \times \log(10000/(10000/(T)))) + (0.450\times300\times((10000/(T))/10000)) + (0.025\times300/1000), \quad \text{eq. S7}$$

where T is the absolute temperature in K.

The thermal lithosphere-asthenosphere boundary (LAB) indicated in Figure 3 in the main text is from Garel et al (2020) and Garel and Thoraval (2021). The large range of temperature covers the LAB in a cooling oceanic lithosphere for a large range of ages (see Garel and Thoraval (2021), for discussion, in particular their Figure 7).

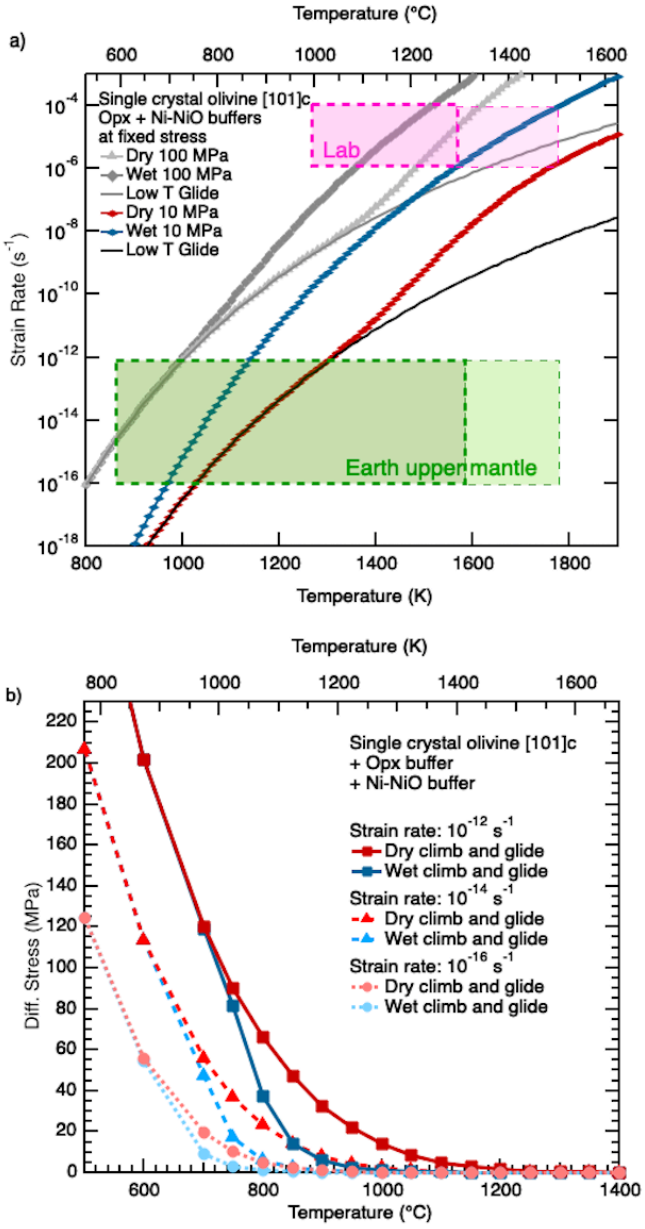

Figure S3: (a) Strain rates as a function of temperature under stress of 100 MPa and 10 MPa for dry and hydrogen-bearing single crystals of olivine deformed in compression. Flow laws

are from Tielke et al. (2017) and Bai et al. (1991). The area in pale pink represents the stress-strain rates field covered by experiments in high temperature (1-atm) creep apparatus (Bai et al., 1991) and the area in pink by Paterson press experiments (e.g., Demouchy et al., 2012; Tielke et al., 2017). The area in pale green represents the field covered by the asthenosphere mantle and in green by the lithospheric mantle, showing the extrapolation of laboratory strain rates to mantle conditions.

References

Bai Q, Mackwell SJ, Kohlstedt DL (1991). High-temperature creep of olivine single crystals. 1. Mechanical results for buffered samples. Journal of Geophysical Research 96:2441–2463

Demouchy S, Bolfan-Casanova N (2016) Distribution and transport of hydrogen in the lithospheric mantle: A review. Lithos 240-243:402–425

Demouchy S, Tommasi A, Barou F, Mainprice D, Cordier P (2012) Deformation of olivine in torsion under hydrous conditions. Physics of the Earth and Planetary Interiors 202-203:57–70

Garel F, Thoraval C (2021) Lithosphere as a constant-velocity plate: Chasing a dynamical LAB in a homogeneous mantle material. Physics if Earth and Planetary Interiors 316: 106710

Garel F, Thoraval C, Tommasi A, Demouchy S, Davies R (2020) Using thermo-mechanical models of subduction to constrain effective mantle viscosity. Earth and Planetary Science Letters 539: 116243

Girard J, Chen J, Raterron P, Holyoke CW (2013) Hydrolytic weakening of olivine at mantle pressure: Evidence of [100](010) slip system softening from single-crystal deformation experiments Physics of the Earth and Planetary Interiors 216:12-20.

Tielke JA, Zimmerman, ME, Kohlstedt DL (2017) Hydrolytic weakening in olivine single crystals. Journal of Geophysical Research 122: 465–3479

5. Data source for Figure 4

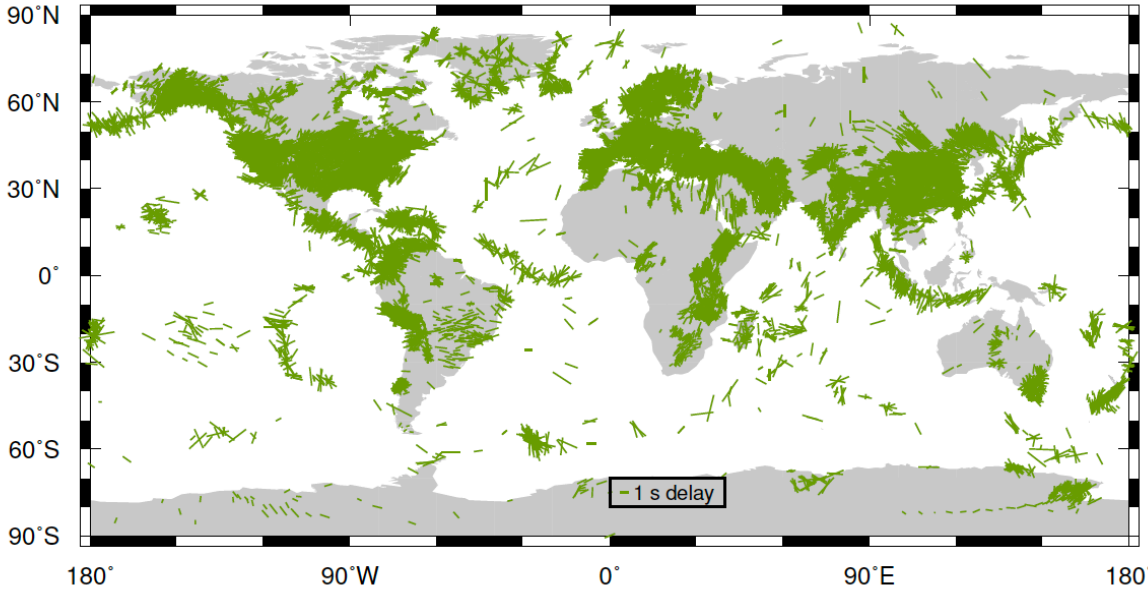

Figure S4. Extractions of the global teleseismic shear-wave splitting database (initiated by Barruol et al. 2009) illustrating seismic anisotropy patterns at the plate scale. Seismic anisotropy is integrated along vertical paths between the core-mantle boundary and the station, with a maximum contribution from the upper mantle. Direction of the bars indicates the direction of polarization of the fast quasi-shear wave and length of the bars shows the delay time between the fast and slow arrivals. This worldwide map shows the extend of the data coverage, but blur the visualization of the mantle flow. Detailed maps are then required, such as the one display in Figure 4. For the references for the plotted splitting data see http://splitting.gm.univ-montp2.fr/DB/public/splittingDB_ref.txt.

References

Barruol G, Wuestefeld A, Bokelmann G (2009) SKS-Splitting-database. Université de Montpellier, Laboratoire Géosciences. https://doi.org/10.18715/sks_splitting_database